Stratospheric X-rays detected at mid-latitudes with a miniaturized balloon-borne microscintillator-PiN diode system

Article

Published Version

It is advisable to refer to the publisher's version if you intend to cite from the work. See [Guidance on citing](#).

www.reading.ac.uk/centaur

Stratospheric X-Rays Detected at Midlatitudes With a Miniaturized Balloon-Borne Microscintillator-PiN Diode System

K. L. Aplin[1] [ID]**, G. J. Marlton[2,3]** [ID]**, and V. Race[1,4]**

[1]Department of Aerospace Engineering, University of Bristol, Bristol, UK, [2]Department of Meteorology, University of Reading, Reading, UK, [3]Now at UK Met Office, Exeter, UK, [4]Now at Huisman Equipment BV, Rotterdam, The Netherlands

Abstract A miniaturized scintillator ("microscintillator"), was flown on a meteorological radiosonde to observe energetic particles in the lower atmosphere. A PiN diode was used to measure the light from the microscintillator to count rates and energies of ionizing radiation from the ground up to the stratosphere (32 km). The flight, over the southern UK on August 27, 2018, occurred during a geomagnetic storm. Low-energy (50–150 keV) particles in the stratosphere were detected in addition to the usual signal from higher-energy cosmic rays. Unusually for these miniaturized radiosonde systems, which are designed to be disposable, the payload was retrieved. This allowed for re-calibration of the microscintillator, which confirmed the low-energy particle detection. Laboratory tests excluded thermal effects on the microscintillator instrument as the origin of the signal. Data from the NOAA POES spacecraft offer the explanation that the microscintillator detected bremsstrahhlung X-rays from energetic electron precipitation (EEP). EEP events may affect weather and climate through a range of physical mechanisms, and this midlatitude observation, well away from the auroral oval, extends the region over which meteorological effects of EEPs need to be assessed. Our findings underline the value of balloon measurements in providing rapid response to space weather events. The energy-discriminating and altitude-sensitive capability of the microscintillator augments spacecraft observations from below.

Plain Language Summary We describe results from flying a miniaturized radiation detector up to 32 km altitude on a weather balloon, in a region of the atmosphere called the stratosphere. The radiation detector was able to measure the energy of the particles it detects in addition to counting them. As well as the counts we expected from high-energy particles entering the atmosphere from space, we also unexpectedly measured some lower-energy particles. Normally the weather balloons are not retrieved, but for this flight we were able to retrieve it and test it again in the lab, confirming that the low-energy particle measurements were real and not due to a problem with the equipment. These low-energy particles are likely to be X-rays which can sometimes enter the atmosphere during periods of enhanced space weather activity. The electrons that are known to produce these X rays were present in enhanced concentrations in near-Earth space, as measured from above by the NOAA POES spacecraft: our measurements are from below. We believe this is the first detection of stratospheric X-rays well away from the polar regions. X-rays affect atmospheric chemistry, which, in turn, to a lesser extent, affects the weather.

1. Introduction

The need to quantify the role of energetic particles in the atmosphere, from both background cosmic radiation and transient space weather events, in weather and climate (e.g., Mironova et al., 2015) is limited by undersampling of key parameters such as ionizing radiation. This has motivated the development of a novel miniaturized ionizing radiation detector, a "microscintillator" with a 0.8 cm^3 CsI(Tl) scintillator crystal coupled to a PiN photodiode in a miniaturized low-power and low-cost package (Aplin et al., 2017). The microscintillator is capable of measuring both the energy and count rate of energetic particles and has previously been calibrated for gamma rays (Aplin et al., 2017). The low mass and power, low cost, and improved performance over other detectors such as Geiger counters make the microscintillator particularly suited for use on meteorological radiosondes, which are not normally retrieved after use.

This paper describes a balloon flight carrying a payload of the microscintillator and two Geiger counters. The flight was unusual for three reasons. Firstly, it serendipitously took place during a geomagnetic disturbance. Secondly, there were unexpected results in the form of low-energy particles in the stratosphere identified by the microscintillator and not the Geigers. Thirdly, enhanced tracking allowed the payload to be retrieved for postflight analysis, validating the findings and allowing the low-energy particles to be associated with energetic electron precipitation, detected at a relatively low geomagnetic latitude (53.9°N), well away from the auroral zone. These electron precipitation events affect atmospheric chemistry (Mironova et al., 2015), are a significant loss term for energetic electrons in the magnetosphere (e.g., Horne et al., 2009), and are now considered as a poorly-understood space weather aviation hazard (Tobiska et al., 2018). In this paper, we describe the flight, its results, and subsequent analysis and interpretation of the data.

2. Test Flight

The microscintillator was integrated with a Vaisala RS92 radiosonde through a bespoke "PANDORA" board (Harrison et al., 2012) which allows data from extra sensors to be sent to the ground in real time over a radio link, in addition to the standard meteorological parameters of pressure, temperature, and humidity. This was a similar approach to that employed by Aplin et al. (2017) for earlier microscintillator flights, with the addition of two LND714 Geiger counters, which have been frequently deployed for balloon-borne energetic particle measurements (Harrison et al., 2014; Makhmutov et al., 2016).

### 2.1. Balloon Launch and Flight Summary

The balloon was launched from Berkeley, in the western UK, (51.69026°N, −2.45741°E) on August 27, 2018 at 18:49 BST. At the time of launch, surface, meteorological conditions were calm with slack winds and a low cloud layer at approximately 2 km. Geomagnetic conditions during the flight were active, with a storm level disturbance at the time of launch identified on the basis of the Dst index (−63 nT) and a Kp index of 5o (Horne et al., 2009; Matzka et al., 2021). The balloon flight was at a geomagnetic latitude of 53.9°N, at a L shell of 2.3.

The launch site was Dr Jenner's House and Garden, a small scientific museum that was formerly the home of vaccination pioneer Dr Edward Jenner, during a public outreach event. Another balloon carrying a standard Vaisala RS92 radiosonde and a balloon tracker with a camera provided by members of the UK High Altitude Society (UKHAS) was launched at 13:00 BST and retrieved by them from London later that day. The ongoing collaboration meant that unusually good tracking was employed for the evening flight, permitting the second balloon's landing location to be accurately identified. (Usually, the radiosonde fails to return data when the balloon is close to the ground because of the lack of line of sight to the receiving station or high signal attenuation, which only allows approximate determination of the landing site, and makes retrieval difficult). This improved tracking allowed the balloon to be located and retrieved the next day 100 km east-south-east of the launch site, in Oxfordshire, UK (51.60336°N, −0.96597°E), having achieved a maximum altitude of 32 km, well into the stratosphere.

2.2. Initial Flight Results

The meteorological data (Aplin, 2021) from the ascending part of the flight are summarized in Figure 1 below (data from the descent are not considered in this paper, but meteorological conditions remained consistent over the full flight trajectory). There was one cloud layer at approximately 2 km altitude, consistent with the broken cloud observations at the launch site. The tropopause was at 178 hPa, 12.5 km. The balloon reached its maximum altitude of 32 km over Fairford, UK, (51.720837°N, −1.784373°E) at 20:47 BST, after which it burst and descended controlled by parachute.

The count rate obtained by the Geigers (Aplin, 2021), Figure 2, showed the classical ionization profile with the mean altitude of the Regener-Pfotzer maximum at 20 ± 2 km, consistent with many previous flights (Harrison et al., 2014). The microscintillator detector count rate (Aplin, 2021) increased with altitude as expected and showed a local maximum at 18 km, consistently with the Geigers. Unlike the Geiger counters, however, the microscintillator's count rate continued to increase with altitude. Both the Geiger

(a) temperature   **(b) pressure**   **(c) relative humidity**
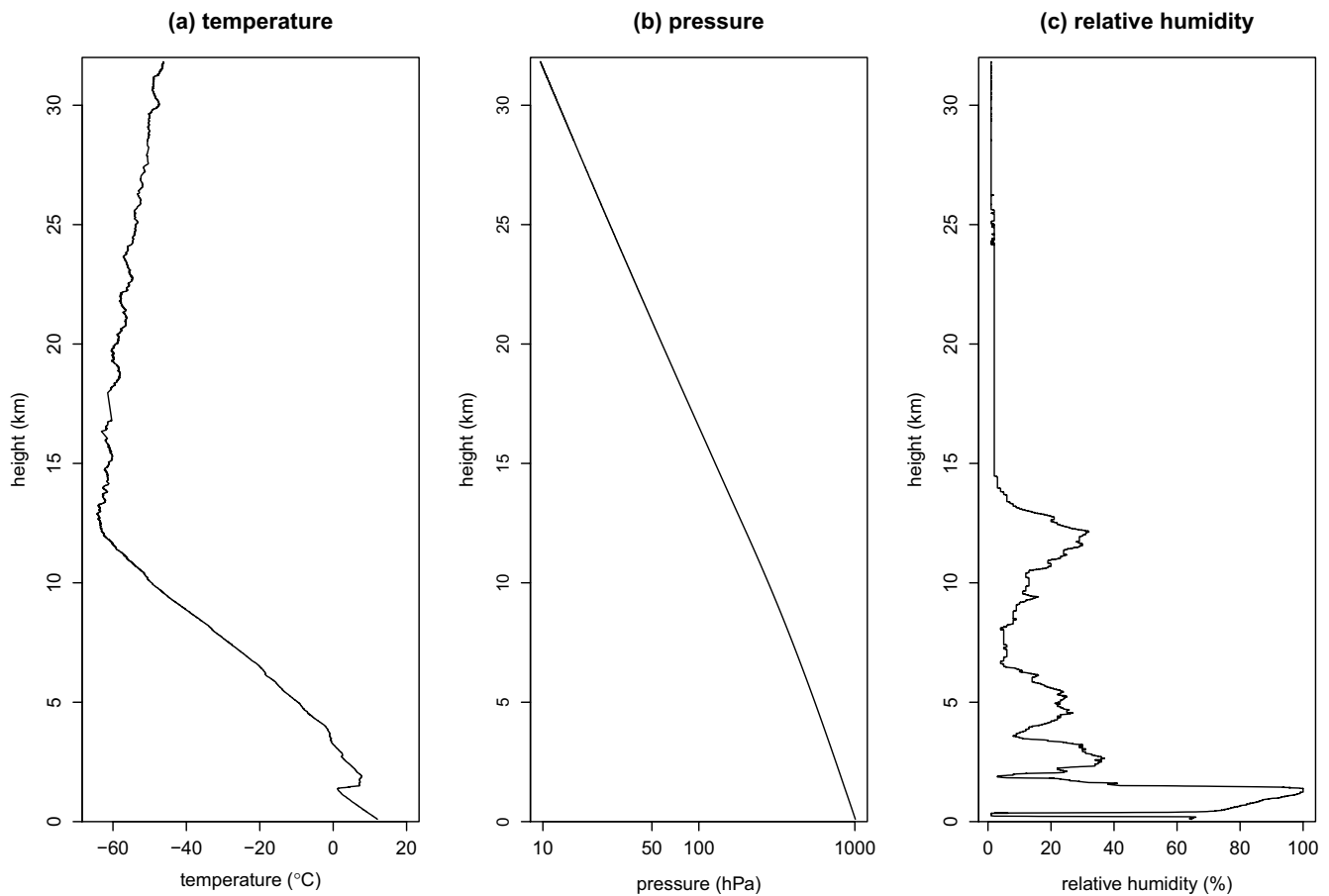
Figure 1. Summary of meteorological data during ascent part of the flight (18:49–20:47 BST) on August 27, 2018. Data are spot measurements sampled every second.

and microscintillator count rates could be validated due to redundancy in the data collected. There were two Geiger counters onboard and their results were consistent (Figure 2a). The microscintillator's default behavior is to output one line of data for every pulse recorded (as for the calibrations described in Aplin et al. [2017]), however, this was not possible for the RS92 radiosonde due to data limitations. Instead, the size of each pulse, which is proportional to the energy deposited in the microscintillator, was calculated using in-flight firmware and placed in one of 10 energy bins (shown in Table 1), with the total number of counts during the recording time interval (typically 30s) also noted. It was therefore possible to compare the total number of counts to the sum of all the counts in each histogram bin. This allowed for missing or corrupt data to be identified and not included in the analysis, on the basis of lack of consistency between each value for total counts. Only data where the count rate was validated in this way are considered in this paper, suggesting that the variability in Figure 2b was not a data retrieval artifact.

It was also possible to use the counts in each energy bin to create an energy spectrum of particles detected by the microscintillator, Figure 3. The strongest feature of the data is the apparent increase in particle energy with altitude. Near the surface, most of the particles are in the 0.6–1 MeV range, which is as expected for terrestrial gamma radiation (e.g., Minty, 1992). In the free troposphere, the energy appears to increase with altitude, and by the tropopause, at 12.5 km most particles are depositing 3.5–6.5 MeV in the detector. In the upper part of the flight, 25–30 km, some particles of higher energy, up to 10 MeV are detected, as well as the reappearance of a significant number of low-energy particles in the C0 channel. The broad increase to higher energy particles with altitude is expected given the increased dominance of secondary cosmic ray particles in the free troposphere and primary cosmic rays above the Pfotzer-Regener maximum at 18–20 km. However, unlike gamma rays, for which well-defined laboratory sources are available, it is not straightforward to calibrate the detector for energetic (>1 GeV) cosmic ray particles. Instead, the energy

(a) Geigers

(b) Microscintillator
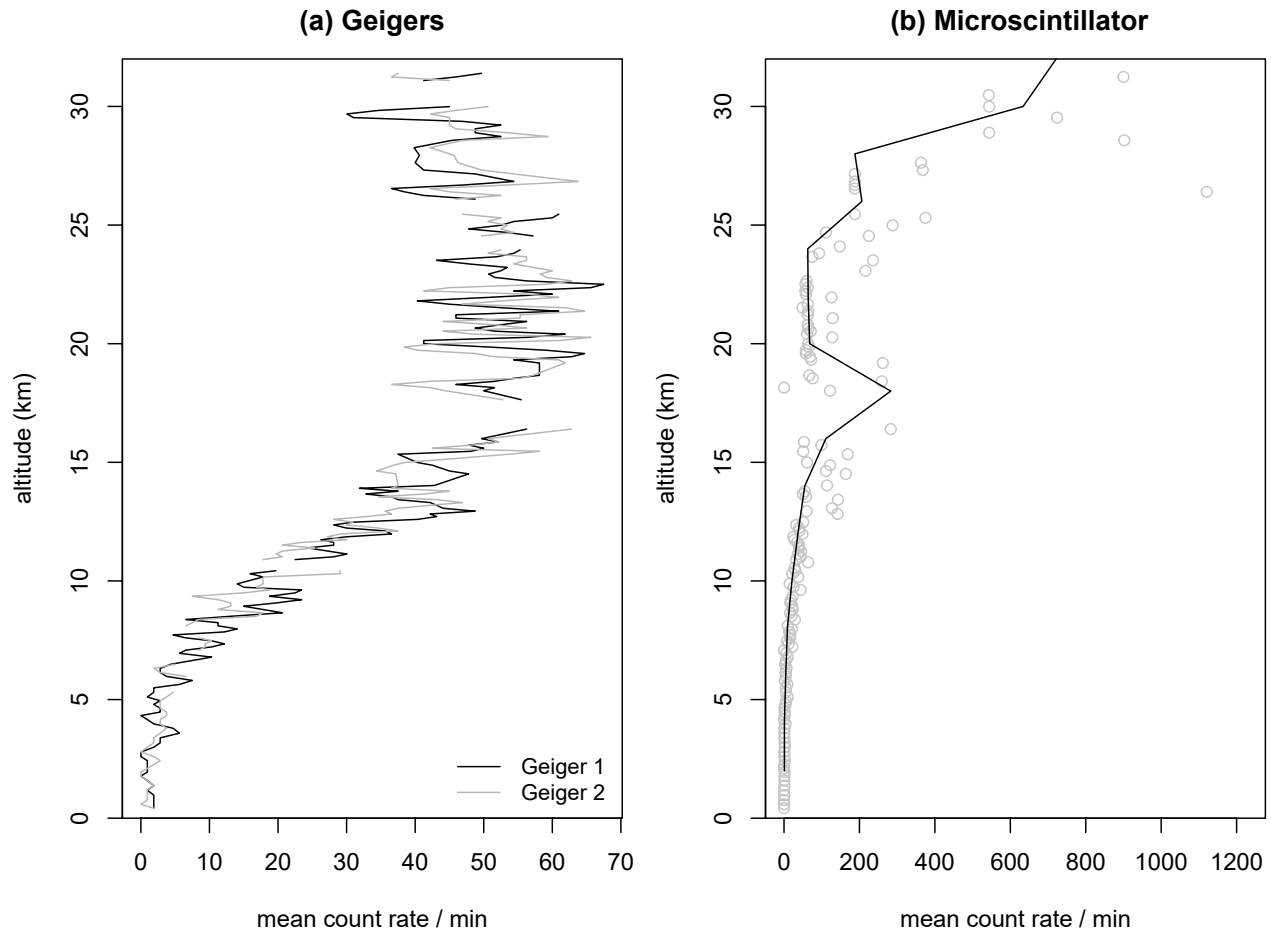
Figure 2. Count rates from energetic particle instruments (a) 1 min averages from LND714 Geiger counters and (b) the microscintillator, with 1 min average count rates plotted as open circles, and 1 km averages shown as a line through the points.

deposited in the detector can be estimated following e.g., Lawrence et al. (2018). Muons and other highly energetic particles such as relativistic protons are typically assumed to be "minimum ionizing particles" and their energy deposition can be calculated on the basis of standard data on stopping power and range in materials (https://pdg.lbl.gov/2014/AtomicNuclearProperties/; Groom et al. [2001]) as they pass through the CsI(Tl) microscintillator crystal with path lengths from 0.8–1.3 cm. The energy deposited is 4.5–7 MeV, consistent with the particle energy most commonly detected in the microscintillator detector as it ascends.

The stratospheric low-energy signal, however, was unexpected. The simplest explanation was that it was an instrumental artifact; for example, whilst previous laboratory experiments verified the instrument continued to perform in a domestic freezer at −20°C, the minimum temperature recorded during this flight was −63°C. Valentine et al. (1993) suggest that the number of photons produced per MeV in CsI(Tl) scintillator at −65°C decreases to about 90% of what it is at 25°C, which would alter the instrument's calibration. Since most of the "low-energy" signals were only observed during the coldest part of the flight, more thorough investigations of the thermal response of the microscintillator instrument were required.

3. Postflight Laboratory Testing

The retrieved microscintillator detector was tested with laboratory gamma ray sources after retrieval, and no difference could be found in its energy sensitivity compared to the pre-flight calibration.

More detailed thermal tests (Aplin, 2021) were carried out on an identical detector, placed (in a protective anti-static bag) onto a basin of dry ice. A K-type thermocouple was taped immediately adjacent to the

Table 1
Energy Binning for Radiosonde

Channel	Min ADC counts	Max ADC counts	Min voltage (mV)	Max voltage (mV)	Min gamma energy (MeV)	Max gamma energy (MeV)	Centered energy (MeV)
C0	0	30	0	146	*0.050*	0.140	0.095
C1	31	50	151	244	0.164	0.605	0.385
C2	51	71	249	347	0.629	1.09	0.861
C3	72	91	352	444	1.12	1.56	1.34
C4	92	112	449	547	1.58	2.05	1.81
C5	113	132	552	645	2.07	2.51	2.29
C6	133	152	649	742	2.54	2.98	2.76
C7	153	173	747	845	3.00	3.47	3.23
C8	174	306	850	1,494	3.49	6.56	5.02
C9	307	1,024	1,499	3,200	6.58	14.7	10.63

Note. The microscintillator firmware placed counts into each bin depending on their pulse size in analog to digital converter (ADC) counts. There were 10 data channels, C0–C9. The maximum ADC value was 1,024 corresponding to a maximum voltage of 5 V from which the pulse size in milliVolts is calculated. The corresponding gamma energy, shown here to three significant figures, is determined from a laboratory calibration technique described in Aplin et al. (2017). The lower energy threshold for C0 is in principle zero, but in practice is determined by the minimum gamma energy that can penetrate the sensor's enclosure, approximately 50 keV, indicated in italics. The center of each energy bin is included for consistency with Figures 3 and 6.

microscintillator, and the temperature recorded manually every 5 min with a thermocouple reader. The thermocouple was checked at the end of each day of measurements by plunging it into the dry ice to check that the anticipated temperature of −66°C was measured accurately. With this setup, a minimum microscintillator temperature of −55°C could be obtained. The entire rig was placed into a lead "castle", with the thermocouple reader outside, to exclude background variability in natural radioactivity. To specifically investigate the detector's energy response with temperature, a bag of potassium chloride was placed within
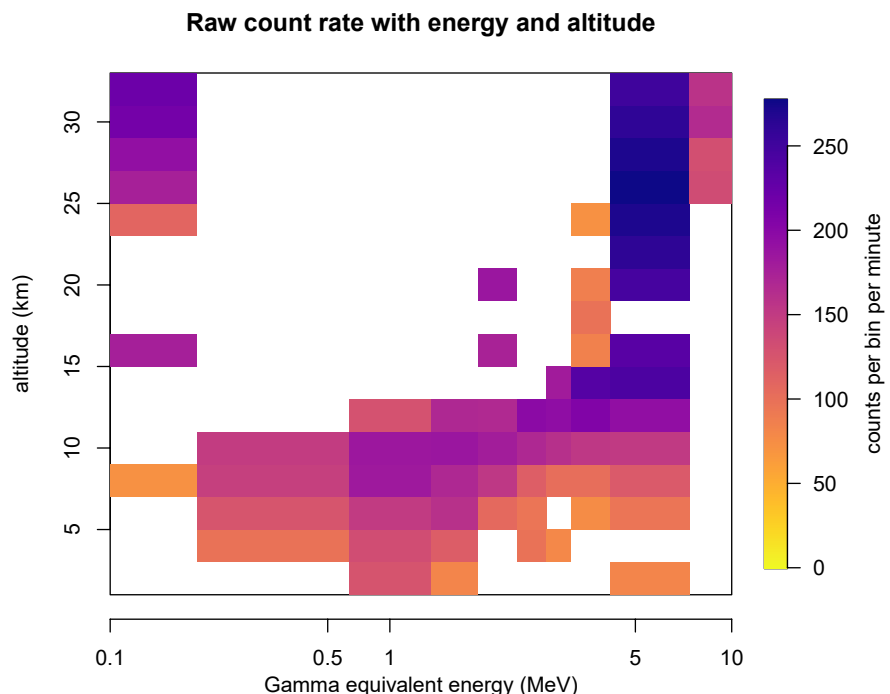
Figure 3. Count rates per energy bin per minute as a function of altitude. Data have been binned into 2 km sections.

(a) +19 degC

n=11555

(b) +5 degC

n=1116

(c) −5 degC

n=1354

(d) −25 to −55 degC

n=1105
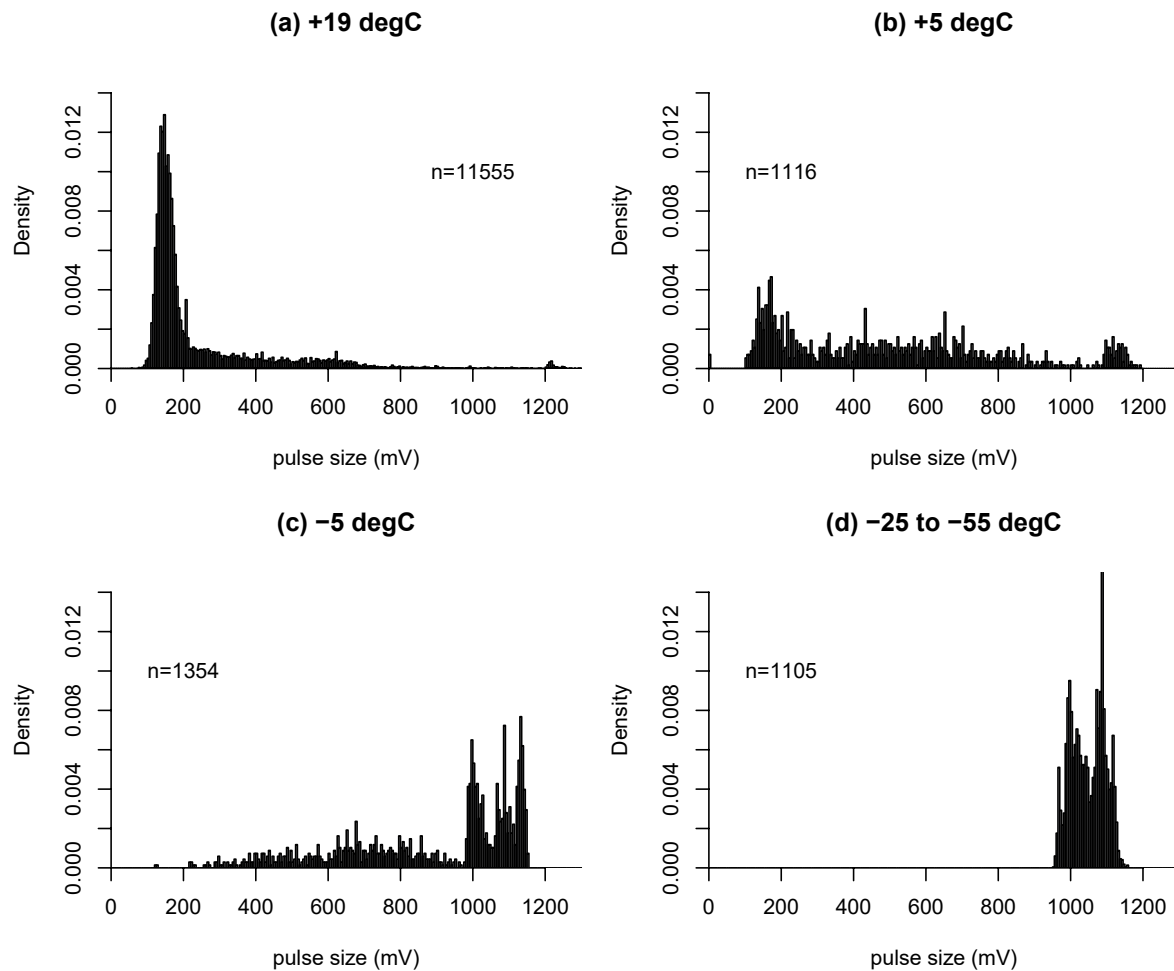
Figure 4. Histograms of pulse size with temperature, showing the fraction of counts in each bin on the abscissa, with the total number of counts *n* in each plot indicated. The histogram bins are 5 mV, arising from the resolution of the microcontroller used. Image in (a) shows a long run (over 3 hr) at room temperature. The images in panels (b) and (c) are obtained for temperatures between 0−10°C and −10−0°C respectively, with the majority of the data within ±1°C of the value stated. The response did not vary for temperatures lower than −20°C, so data were combined for (d).

the lead castle above the detector. Potassium naturally contains 0.012% of the radioisotope ^{40}K which emits a characteristic gamma ray at 1.46 MeV (Chu et al., 1999), allowing KCl to be used as a low-level radioactive source (e.g., Kawano, 2006). ^{40}K also emits low-energy beta radiation (electrons) which can be excluded by placing a thin sheet of aluminum between the KCl and microscintillator. With this apparatus, it was possible to take data whilst the temperature remained fairly constant. For example, almost all the measurements recorded as being at −5°C in Figure 4b below were taken at temperatures between −4 and −6°C. Data were recorded via a USB cable passed through a hole in the lead castle, and connected to a computer serial interface. The instrument continued to function at temperatures down to at least −55°C.

Figure 4a shows the response at room temperature. The major broad peak at 160 mV dropping off to a "shoulder" from 200−700 mV arises from a combination of the background radiation and the scintillator′s quantum efficiency, that is, the fraction of gammas depositing all their energy in the detector that are detected, which decreases from a maximum of almost 100% at 200 keV down to 7% for energies >5 MeV (Aplin et al., 2017). For the device used in these tests, the lowest energy detectable is ∼50 keV due to the scintillator's enclosure. Following an established detailed calibration methodology (Aplin et al., 2017), narrower peaks from natural radioisotopes can be seen superposed on this background. For example, at 200 mV (^{214}Bi; 0.61 MeV, ^{208}Tl; 0.58 MeV), 417.5 mV (^{40}K; 1.33 MeV) and 622.5 mV (^{208}Tl; 2.61 MeV) (Minty, 1992). The small peak at the far right side of the plot corresponds to ∼6 MeV deposited in the detector by muons. Figures 4b–4d show that the broad peak at 160 mV appears to shift to higher energy as the detector cools

down. There are two potential reasons for this thermal effect. First, it could be caused by a change in the sensitivity of the detector, i.e., the relationship between pulse size and particle energy in mV/keV. Second, changes in the quantum efficiency would modify the shape of the distribution even with a constant background, by varying the number of particles detected at each energy. Either or both of these effects could be occurring in the data shown in Figure 4. One way to identify if the sensitivity of the detector is changing with temperature is to identify a peak, for example, from the ^{40}K source, and note whether the pulse size (voltage) associated with it changes with temperature. Figure 4b suggests that the peaks identified in Figure 4a at 200, 417.5, and 622.5 mV (^{214}Bi/^{208}Tl, ^{40}K and ^{208}Tl, respectively, Aplin et al. [2017]) remain above the noise at 5°C, indicating that there is not a substantial change in the detector's energy sensitivity at this temperature. There were insufficient counts at the lower temperatures shown in Figures 4c and 4d to clearly resolve these gamma peaks above the noise.

Additional experiments were, therefore, run in a domestic fridge at 5°C and a freezer at −18°C (Aplin, 2021). These remain at a constant temperature, allowing the equipment to be left for longer periods of time than the data shown in Figure 4. In this experiment data were logged using the microscintillator's Bluetooth output rather than with a cable, to ensure a stable temperature regime. No lead castle was used, to enhance the peaks from natural radioactivity. The longer duration of these experiments allowed specific peaks to be identified at cooler temperatures, as shown in Figure 5. Spectral peaks from ^{40}K and ^{208}Tl are well above the noise in Figures 5a–5c, indicating that cooling produces no detectable change in the microscintillator's energy sensitivity. A thermal response in the sensitivity is expected for this type of scintillator due to the changing number of photons emitted per unit of deposited energy (e.g., Valentine et al., 1993), but this was not seen in our experiments. It is possible that the sensitivity change is undetectable to within the 5 mV pulse size resolution of the microscintillator, which is currently limited by the analog to digital converter used in the on-board microcontroller. Further experiments are planned to better understand thermal effects on the instrument's energy calibration.

Cooling does however noticeably change the microscintillator's quantum efficiency, resulting in a shifting background shape. The relative pulse heights of the radioisotopes also change in Figure 5, demonstrating that the detector gets more efficient at detecting higher-energy particles as it cools. For example, the ^{40}K peak at 622.5 mV which is just above the background in Figure 5a, grows in height from Figures 5b and 5c, further supporting the idea that quantum efficiency is temperature-sensitive.

The key conclusion from these laboratory tests is that no change in the microscintillator's energy calibration with temperature has been observed. Detection of the low-energy 50–150 keV particles in the stratosphere is therefore highly likely to be robust. However, the enhanced signal at energies ∼5 MeV apparent in Figure 3 is more likely to be an instrument artifact resulting from a change in efficiency with temperature. In the next section, the flight data are reanalyzed using insights from the postflight testing.

## 4. Reanalysis of Flight Data and Discussion

The experiments described above revealed that some of the counts in the results shown in Figure 3 were likely to be due to a temperature-dependent shift in the background radiation, as the detector ascended to cooler regions of the atmosphere (Figure 1). Figure 4 shows that as the detector cools, the broad "background" peak shifts to the right, an effect shown in Section 3 to be due to quantum efficiency. The high count rates at energies around 5 MeV in Figure 3 are therefore expected to be partially due to the detector's thermal background response, which should be subtracted to reveal the presence of peaks from energetic particles. The data shown in Figure 4 were used to generate a background spectrum for each 10°C air temperature range experienced on the weather balloon, to subtract from its measurements, Figure 6. Implementation of this procedure is explained in Supporting Information S1. It should be noted that this thermal sensitivity of quantum efficiency only has a significant effect on the high-energy particles detected, and the low-energy signal at ∼100 keV is relatively unaffected. If, as seems likely from Figures 4 and 5, quantum efficiency improves for higher-energy particles at lower temperatures, the effect on the low-energy particles would be that detection remained robust, but their count rates were underestimated.

Figure 6 shows the underlying particle energies after subtraction of the thermally-dependent background signal. The low-energy particles, which make up the majority of the counts above 24 km altitude remain
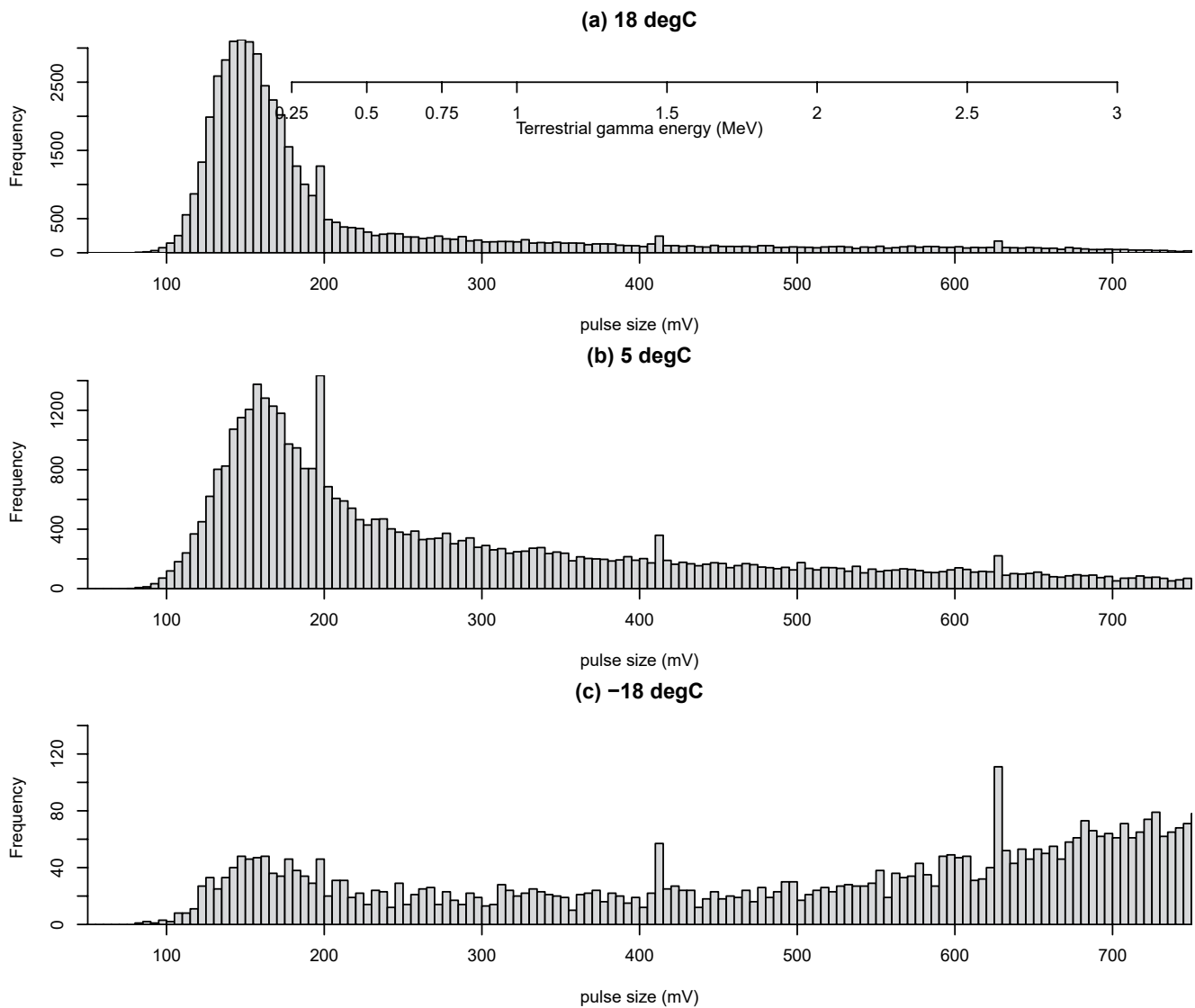
Figure 5. Microscintillator response, showing the number of counts in each bin against pulse size in 5 mV bins at (a) room temperature, with an additional *x*-axis added to show the calibration to gamma energy (b) in a domestic refrigerator at 5°C and (c) in a domestic freezer at −18°C. Spectral lines from terrestrial gamma radiation (<3 MeV; Baldoncini et al. [2017]) at 187.5, 417.5, and 622.5 mV visible in (a) from ^{214}Bi, ^{40}K, and ^{208}Tl occur at the same voltages in a, b, and c, demonstrating no detectable thermal changes in the instrument's energy sensitivity.

present. The laboratory experiments demonstrated that the microscintillator's quantum efficiency at detecting particles in its lower energy range decreased as temperature decreased, indicating that there must have been many particles present for any to be counted at all. Above the altitude of the Regener-Pfotzer maximum (Figure 2b), the microscintillator count rate increases, inconsistently with the Geigers. This is most likely due to the LND714 Geiger tubes used being optimized for higher-energy photons. Efficient detection of low-energy photons with a Geiger tube requires a mica window and a fill gas of high atomic number (xenon or krypton) (Knoll, 1989) rather than the neon fill gas and stainless steel construction of the LND714 tube. Away from the low-energy stratospheric signal, the particle energy generally increases with altitude. Other than this lower-energy signal, the data are consistent with previous flights (Aplin et al., 2017; Harrison et al., 2014), but it is difficult to provide a detailed explanation since many other particles in the cosmic ray cascade, for which the detector is not yet calibrated or modeled, are present and the nature of the signal they will produce is unclear.

Corrected count rate with energy and altitude
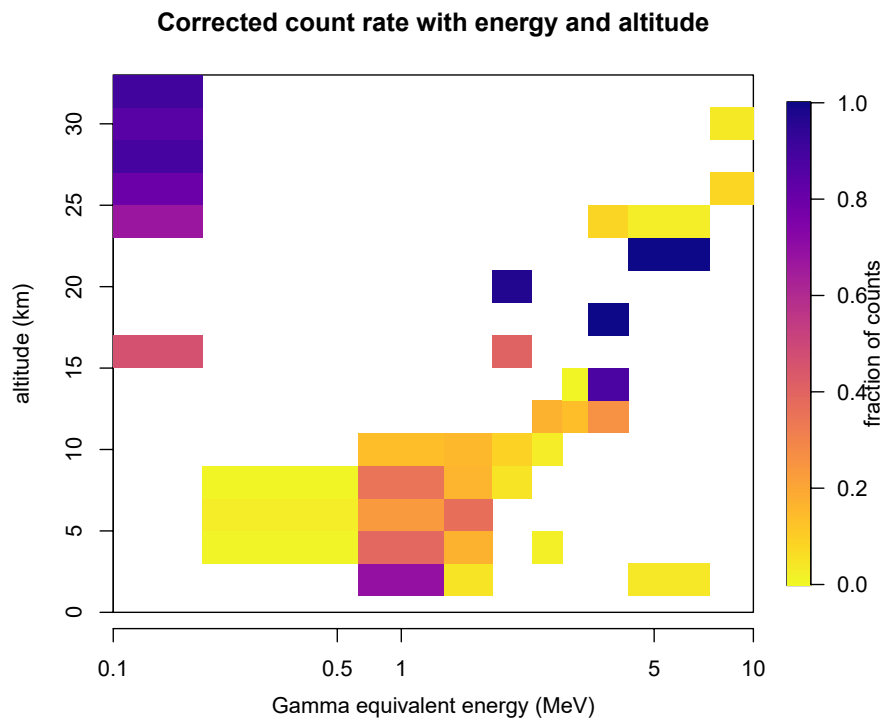
Figure 6. Relative count rates per energy bin per minute as a function of altitude. Data have been binned into 2 km sections. These data have been corrected to subtract the background, which varies with temperature, using a procedure described in Supporting Information S1.

The geomagnetic storm during the flight on August 27, 2018 provides a clue to the origin of the unexpected low-energy signal. During geomagnetic storms electrons trapped in the Van Allen belts are accelerated and precipitate into the upper atmosphere, which is called "energetic electron precipitation" (EEP), (sometimes called "relativistic electron precipitation" or "electron precipitation events" e.g., Millan & Thorne, 2007; Mironova et al., 2015). The electrons cannot penetrate into the stratosphere but the Bremsstrahlung X rays they generate can descend to altitudes of ~20 km, and have been detected by previous balloon flights at similar altitudes over auroral regions (e.g., Berger & Seltzer, 1972; Makhmutov et al., 2016; Smith et al., 1995). These photons ionize the air, producing electrons, as described in the references above and quantified by e.g., Xu et al. (2017). Atmospheric effects of EEP are complex, involving a range of mechanisms, and studies tend to agree qualitatively, but not quantitatively, that the ionization from both the X rays and their secondary electrons could lead to weather and climate effects potentially detectable at the surface (Mironova et al., 2015). The anomalous low-energy signals detected by the microscintillator during the geomagnetic disturbance could be either Bremsstrahlung X rays themselves or secondary electrons created by the X rays through photoelectric absorption or Compton scattering. The two flights reported in Aplin et al. (2017), also from the southern UK, with an identical microscintillator under geomagnetically quiet conditions did not observe these low-energy particles, suggesting that they are not routinely created by the cosmic ray background.

The suggestion that Bremsstrahlung X rays created by energetic precipitating electrons were present in the atmosphere on August 27, 2018 is supported by observations from the NOAA POES satellites (POES Data Access, 2021). These satellites are in low earth orbit, at an altitude of approximately 780 km, and carry identical detectors to monitor energetic particle precipitation. The most relevant instrument for this study is the Medium Energy Proton Detector (MEPED) which, as well as detecting protons, responds to electrons expected to produce Bremsstrahlung (Sørass et al., 2018; Yando et al., 2011). Each satellite carries two perpendicular MEPED instruments defined as 0° and 90° (Sørass et al., 2018). Two bursts of precipitating electrons occurred within the balloon sensor's time aloft, which were detected by both 0° and 90° MEPED instruments in channels E1-3, corresponding to electrons with energies >30, 100, and 300 keV respectively

(Sørass et al., 2018). The first burst, detected by both POES15 and POES19 approximately coincided (to <200s) with the detection of low-energy particles by the balloon at 15 km shown in Figure 6. A second, stronger (double the flux of the first electron burst), electron precipitation event was recorded by POES18, which is consistent with the stronger detection of low-energy photons by the balloon sensor above 23 km. During both these precipitation events the ground tracks of both POES15 and POES18 were in a geographically similar region to the balloon, over the Northern Atlantic between the UK and Iceland.

The microscintillator's count rate of low-energy (∼100 keV) particles can be estimated as 10-20 $cm^{-2}s^{-1}$ from Figure 2b, assuming that 100% of the total counts recorded were from C0, on the basis of Figure 6. Note that as the lab experiments (see Figure 4b) suggest that the scintillator has a lower quantum efficiency at ∼100 keV for temperatures <−25°C, the actual flux may be considerably higher than the measured count rate. It seems likely that the microscintillator detected Bremsstrahlung X rays, as the energy range is consistent with photons of >0.3 MeV penetrating to an altitude of ∼30 km (Berger & Seltzer, 1972; Makhmutov et al., 2003). The count rates are also consistent with models and the POES data (Xu & Marshall, 2019).

Unfortunately, the lack of spectral resolution from the flight prevents the estimation of the energy of incoming electrons in for example, Makhmutov et al. (2016) or Smith et al. (1995). Magnetospheric electrons in the radiation belts are usually only measured by satellites, hence EEP characteristics detected as a function of altitude within the atmosphere can provide valuable additional information on electron losses from the magnetosphere.

5. Conclusions

In the balloon flight described here, a novel microscintillator-Geiger payload was flown to 32 km altitude during a geomagnetic storm. The ionizing radiation measured by the independent sensors was consistent up to the Regener-Pfotzer maximum, but above this altitude, the microscintillator's count rate increased with altitude, unlike the Geiger counters. Additionally, the microscintillator unexpectedly measured particles with energies ∼100 keV. Re-calibration and thermal testing of the retrieved payload validated this finding. The characteristics of the lower-energy particles are consistent with Bremsstrahlung X rays originating from precipitating electrons (or subsequent photo-/Compton electrons) measured at 780 km by the MEPED instrument on the NOAA POES15, 18 and 19 satellites which were over the Northern Atlantic at the same time as the balloon flight. The increase in microscintillator count rate above 20 km, recorded independently of the spectral information, is not consistent with the Geiger results, but this is explained by the insensitivity of the Geiger counters to lower-energy particles.

There are many balloon measurements of EEP in the auroral zone, and at the poles (e.g., Parks et al., 1993; Woodger et al., 2015), but this appears to be the first reported observation in the mid-geomagnetic latitudes, well outside the auroral oval. Further flights, with the improved spectral resolution, are needed to assess the frequency of these midlatitude EEPs, the energy of their parent electrons, and any role in atmospheric chemistry. As pointed out by Bazilevskaya et al. (2021), the CMIP6 climate model does not account for ionization below an altitude of 50 km, which may lead to an under-estimation of chemical effects of EEP at lower altitudes.

Balloons carrying low-cost and miniaturized instruments provide an effective way to investigate high-energy particles in the atmosphere, as these findings demonstrate. Routinely-launched meteorological balloon systems in particular offer opportunities for coordinated and rapid-response multi-site campaigns which provide new atmospheric data that augment spacecraft data from below. Newer meteorological radiosonde systems permit greater data transfer, allowing the energy associated with individual pulses to be recorded, vastly improving the energy resolution. Balloons provide additional information in the data-sparse region between spacecraft and ground-based observations. Unlike larger balloon campaigns (e.g., BARREL; Woodger et al. [2015]), smaller balloon systems can measure an altitude profile of energetic particles, which is necessary to understand their precipitation into the atmosphere (Xu et al., 2017).

Conflict of Interest

The authors declare no conflicts of interest relevant to this study.

Data Availability Statement

Data are stored at the University of Bristol data repository, data.bris and are cited in the text as Aplin (2021). NOAA satellite data are also cited in the text as POES Data Access (2021).

References

Aplin, K. L. (2021). *Balloon data*. University of Bristol Data Repository. https://doi.org/10.5523/bris.25hgq8mkeef6c2flnyon8l1xv4

Aplin, K. L., Briggs, A. A., Harrison, R. G., & Marlton, G. J. (2017). Measuring ionizing radiation in the atmosphere with a new balloon-borne detector. *Space Weather*, *15*, 663–672. https://doi.org/10.1002/2017SW001610

Baldoncini, M., Albéri, M., Bottardi, C., Minty, B., Raptis, K. G., Strati, V., & Mantovani, F. (2017). Exploring atmospheric radon with airborne gamma-ray spectroscopy. *Atmospheric Environment*, *170*, 259–268. https://doi.org/10.1016/j.atmosenv.2017.09.048

Bazilevskaya, G. A., Dyusembekova, A. S., Kalinin, M. S., Krainev, M. B., Makhmutov, V. S., Svirzhevskaya, A. K., et al. (2021). Comparison of the results on precipitation of high-energy electrons in the stratosphere and on satellites. *Cosmic Research*, *59*(1), 24–29. https://doi.org/10.1134/s0010952521010020

Berger, M. J., & Seltzer, S. M. (1972). Bremsstrahlung in the atmosphere. *Journal of Atmospheric and Terrestrial Physics*, *34*(1), 85–108. https://doi.org/10.1016/0021-9169(72)90006-2

Chu, S. Y. F., Ekström, L. P., & Firestone, R. B. (1999). *The Lund/LBNL nuclear data search, version 2.0*. Retrieved from http://nucleardata.nuclear.lu.se/toi/

Groom, D. E., Mokhov, N. V., & Striganov, S. (2001). Muon Stopping-Power and Range Tables, 10 MeV-100 TeV. *Atomic Data and Nuclear Data Tables* (Vol. 78). https://doi.org/10.1006/adnd.2001.0861

Harrison, R. G., Nicoll, K. A., & Aplin, K. L. (2014). Vertical profile measurements of lower troposphere ionisation. *Journal of Atmospheric and Solar-Terrestrial Physics*, *119*, 203–210. https://doi.org/10.1016/j.jastp.2014.08.006

Harrison, R. G., Nicoll, K. A., & Lomas, A. G. (2012). Note: Programmable data acquisition system for research measurements from meteorological radiosondes. *Review of Scientific Instruments*, *83*(3), 036106. https://doi.org/10.1063/1.3697717

Horne, R. B., Lam, M. M., & Green, J. C. (2009). Energetic electron precipitation from the outer radiation belt during geomagnetic storms. *Geophysical Research Letters*, *36*, L19104. https://doi.org/10.1029/2009GL040236

Kawano, T. (2006). Potassium chloride radiation sources fabricated by compressing and forming method. *Radiation Safety Management*, *5*(1), 5–11. https://doi.org/10.12950/rsm2002.5.5

Knoll, G. F. (1989). *Radiation detection and measurement* (2nd ed.). John Wiley and Sons.

Lawrence, D. J., Fix, S., Goldsten, S. O., Heuer, S. V., Hourani, R. S., Kerem, S., & Peplowski, P. N. (2018). Near-space operation of compact CsI, CLYC, and CeBr₃ sensors: Results from two high-altitude balloon flights. *Nuclear Instruments and Methods in Physics Research A*, *905*, 33–46. https://doi.org/10.1016/j.nima.2018.07.026

Makhmutov, V. S., Bazilevskaya, G. A., & Krainev, M. B. (2003). Characteristics of energetic particle precipitation into the earth's polar atmosphere and geomagnetic conditions. *Advances in Space Research*, *31*(4), 1087–1092. https://doi.org/10.1016/s0273-1177(02)00814-1

Makhmutov, V. S., Bazilevskaya, G. A., Stozhkov, Y. I., Svirzhevskaya, A. K., & Svirzhevsky, N. S. (2016). Catalogue of electron precipitation events as observed in the long-duration cosmic ray balloon experiment. *Journal of Atmospheric and Solar-Terrestrial Physics*, *149*, 258–276. https://doi.org/10.1016/j.jastp.2015.12.006

Matzka, J., Stolle, C., Yamazaki, Y., Bronkalla, O., & Morschhauser, A. (2021). The geomagnetic Kp index and derived indices of geomagnetic activity. *Space Weather*, *19*(5), e2020SW002641. https://doi.org/10.1029/2020SW002641

Millan, R. M., & Thorne, R. (2007). Review of radiation belt relativistic electron losses. *Journal of Atmospheric and Solar-Terrestrial Physics*, *69*(3), 362–377. https://doi.org/10.1016/j.jastp.2006.06.019

Minty, B. R. S. (1992). Airborne gamma-ray spectrometric background estimation using full spectrum analysis. *Geophysics*, *57*(2), 279–287. https://doi.org/10.1190/1.1443241

Mironova, I. A., Aplin, K. L., Arnold, F., Bazilevskaya, G. A., Harrison, R. G., Krivolutsky, A. A., et al. (2015). Energetic particle influence on atmospheric processes. *Space Science Reviews*, *194*(1), 1–96. https://doi.org/10.1007/s11214-015-0185-4

Parks, G. K., Freeman, T. J., Mccarthy, M. P., & Werden, S. H. (1993). *The discovery of auroral X-rays by balloon-borne detectors and their contributions to magnetospheric research* (Vol. 80, pp. 17–23). American Geophysical Union Geophysical Monograph Series.

POES Data Access. (2021). Retrieved from https://www.ngdc.noaa.gov/stp/satellite/poes/dataaccess.html

Smith, D. M., Lin, R. P., Anderson, K. A., Hurley, K., & Johns, C. M. (1995). High-resolution spectra of 20-300 keV hard X-rays from electron precipitation over Antarctica. *Journal of Geophysical Research: Space Physics*, *100*(A10), 19675–19685. https://doi.org/10.1029/95ja01472

Sørass, F., Sandanger, M., & Smith-Johnsen, C. (2018). NOAA POES and MetOp particle observations during the 17 March 2013 storm. *Journal of Atmospheric and Solar-Terrestrial Physics*, *177*, 115–124. https://doi.org/10.1016/j.jastp.2017.09.004

Tobiska, W. K., Didkovsky, L., Judge, K., Weiman, S., Bouwer, D., Bailey, J., et al. (2018). Analytical representations for characterizing the global aviation radiation environment based on model and measurement databases. *Space Weather*, *16*(10), 1523–1538. https://doi.org/10.1029/2018sw001843

Valentine, J. D., Moses, W. W., Derenzo, S. E., Wehe, D. K., & Knoll, G. F. (1993). Temperature dependence of CsI(Tl) gamma-ray excited scintillation characteristics. *Nuclear Instruments and Methods in Physics Research A*, *325*, 147–157. https://doi.org/10.1016/0168-9002(93)91015-f

Woodger, L. A., Halford, A. J., Millan, R. M., McCarthy, M. P., Smith, D. M., Bowers, G. S., et al. (2015). A summary of the BARREL campaigns: Technique for studying electron precipitation. *Journal of Geophysical Research: Space Physics*, *120*(6), 4922–4935. https://doi.org/10.1002/2014ja020874

Xu, W., & Marshall, R. A. (2019). Characteristics of energetic electron precipitation estimated from simulated bremsstrahlung X-ray distributions. *Journal of Geophysical Research: Space Physics*, *124*(4), 2831–2843. https://doi.org/10.1029/2018ja026273

Xu, W., Marshall, R. A., Fang, X., Turunen, E., & Kero, A. (2017). On the effects of bremsstrahlung radiation during energetic electron precipitation. *Geophysical Research Letters*. https://doi.org/10.1002/2017G:076510

Yando, K., Millan, R. M., Green, J. C., & Evans, D. S. (2011). A Monte Carlo simulation of the NOAA POES medium energy proton and electron detector instrument. *Journal of Geophysical Research: Space Physics*, *116*(A10). https://doi.org/10.1029/2011ja016671